DOI:10.1111/cgf.14072
Eurographics Symposium on Geometry Processing 2020
Q. Huang and A. Jacobson
(Guest Editors)

Volume 39 (2020), Number 5

A parametric analysis of discrete Hamiltonian functional maps

E. Postolache[1], M. Fumero[1], L. Cosmo[1,2] and E. Rodolà[1]

[1]Sapienza University of Rome
[2]University of Lugano

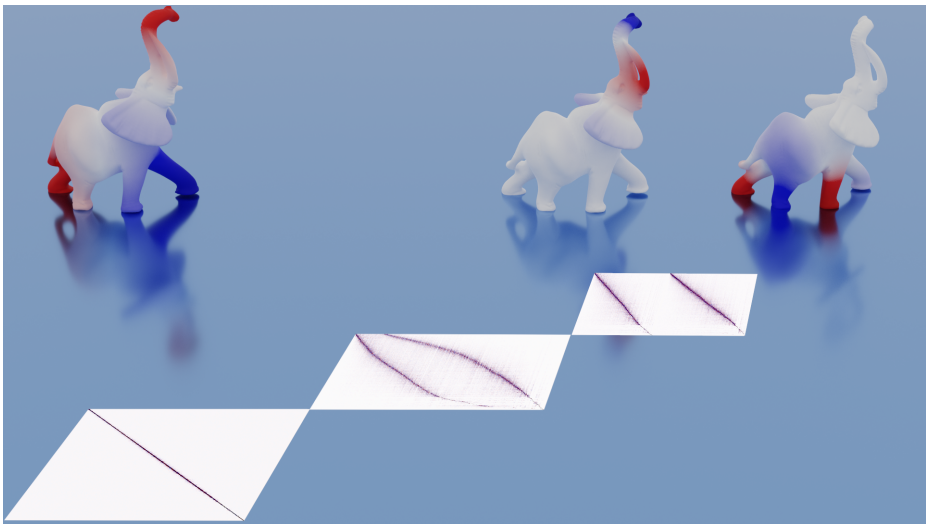

Figure 1: *The fourth Laplacian eigenfunction on the elephant (left) is separated into components residing on complementary parts (right) by the action of a discrete Hamiltonian operator whose step potential has support only on the elephant's body (i.e. head excluded). The separation from the Laplacian eigenbasis is the result of continuous perturbations of the potential energy and is captured by Hamiltonian functional maps, with a bi-diagonal slanted structure. When the potential is low, a Hamiltonian map is simply the identity (bottom left). Increasing the energy the diagonal separates (center map) and at convergence the bi-diagonal structure emerges (top right).*

Abstract

In this paper we develop an in-depth theoretical investigation of the discrete Hamiltonian eigenbasis, which remains quite unexplored in the geometry processing community. This choice is supported by the fact that Dirichlet eigenfunctions can be equivalently computed by defining a Hamiltonian operator, whose potential energy and localization region can be controlled with ease. We vary with continuity the potential energy and study the relationship between the Dirichlet Laplacian and the Hamiltonian eigenbases with the functional map formalism. We develop a global analysis to capture the asymptotic behavior of the eigenpairs. We then focus on their local interactions, namely the veering patterns that arise between proximal eigenvalues. Armed with this knowledge, we are able to track the eigenfunctions in all possible configurations, shedding light on the nature of the functional maps. We exploit the Hamiltonian-Dirichlet connection in a partial shape matching problem, obtaining state of the art results, and provide directions where our theoretical findings could be applied in future research.

CCS Concepts

• ***Computing methodologies*** → *Spectral methods; Shape analysis;*

1. Introduction

In the last decades, spectral geometry processing has been a very active field of research in computer graphics. Spectral methods in shape processing tasks provide a meaningful way to capture intrinsic geometric information, otherwise difficult to access. The discrete Laplace-Beltrami operator plays a major role in such context, finding countless applications such as shape retrieval [RWP06, GMT15], shape compression [KG01], shape reconstruction [BEKB15, CPR*19], and shape matching [OBCS*12, KBB*13, GCR*17] to name but a few. More recently, there has been an increase of attention on topics that deal with *partiality* [RCB*17, CRB*16, RCL*17, CRM*16], where a useful alternative to the Laplacian has been found in the discrete Hamiltonian operator [MRCB17, CSBK18, RTO*19, RLB*19]. This operator, whose continuous counterpart is employed extensively in different branches of physics and chemistry, makes of its localization properties the principal reason for its introduction in the field. What is still missing, is an in-depth study on the connection between the Laplacian and Hamiltonian operators and their associated eigenbases. Providing a solid theoretical framework concerning this relation is required in order to obtain a broader view on the range of possible applications in spectral geometry processing. We show that this connection can indeed be established, through the analysis of the parametric behavior of the Hamiltonian via continuous spectral perturbations, both at a local differential level and at an asymptotic (and thus more global) level, manifested in the functional maps between the associated eigenbases. Encouraged by these theoretical results we present a first example of application that reaches results at the state of the art for the task of partial shape matching.

2. Related work

Shape analysis

The Laplace-Beltrami operator (LBO) is ubiquitous in computer graphics [GSS99, Tau95, Lev06] and has been employed in many applications such as shape retrieval [RWP06, GMT15], shape compression [KG01], and shape matching [OBCS*12, KBB*13]. The first examples of localized harmonics in shape analysis have been obtained through compressed manifold modes [OLCO13, NVT*14, KGB16], a construction of local orthogonal bases that approximately diagonalize the Laplacian.

More recently, the Hamiltonian operator has been introduced in the shape analysis community by [MRCB17, CSBK18], where the authors analyze it for the first time from a discrete geometric point of view. The Hamiltonian has the unique property of localizing harmonics on arbitrary subsets of manifolds by exploiting step potential functions defined on the domain. Potential functions are employed also in [LJC17] to account for boundary conditions of Dirac eigenfunctions. [RTO*19] exploited the Hamiltonian operator to perform region localization without the need to explicitly seek for a map.

We rely on these preliminary results, and further extend the theoretical knowledge by studying the parametric behavior of the Hamiltonian operator, while relating its eigenfunctions to those of the Laplace-Beltrami operator. In addition, we provide some mathematical results that can clarify its precise behavior, especially when the discrete setting limits the behavior of its continuous counterpart.

Functional maps

The functional map formalism was introduced in [OBCS*12] to find correspondences between near-isometric manifolds. The framework exploits linear maps between functional spaces, where typically Laplacian eigenbases are used to represent functions.

In the partial setting, the relationship between Laplacian eigenfunctions on a full shape and harmonics on isometrically deformed subsets has been investigated in [RCB*17] using Neumann boundary conditions. The analysis was performed using perturbation analysis on a block-diagonal Laplacian matrix. The relationship is given by a functional map represented by a slanted-diagonal matrix, relating its slope to the area of the submanifold. This information was used as a prior in order to extend the functional maps pipeline and perform partial shape matching. Differently, here we investigate the functional relationship between the Hamiltonian eigenbasis and the LBO eigenbasis, defined with Dirichlet boundary conditions, and advocate its use in geometry processing tasks. Along this line, we build a new pipeline for partial shape matching obtaining results that are in line with the state of the art. This underlines the fact that the Neumann basis is not the only possible choice for this type of task.

Structural mechanics

Mechanical engineering has long been a source of inspiration for researchers in shape analysis. The most important tool borrowed from this field is certainly the Finite Element Method [ZTZ13], used for obtaining linear algebraic discretizations of continuous differential equations efficiently. Modern shape analysis employs spectral methods for a wide range of tasks, and since spectral quantities are central to the study of dynamical systems and vibrating phenomena, there is a rich interaction between the two fields.

In the proposed theoretical analysis, we will investigate how eigenpairs (otherwise called modes) evolve when varying the step potential parameter τ in the Hamiltonian with continuity. There exists a vast literature in the structural mechanics field that studies modal interactions. The first experimental observations in the 1960s were related to simple vibrating objects such as cantilever plates [CT62]. Perkins and Mote [PM86] used perturbation analysis on linear operators to explain different types of modal interactions in a general continuous setting, proving that this behavior is not a discretization byproduct. An important type of modal interaction studied in these papers is the veering interaction [dBAL09, DBAL07], characteristic of self-adjoint operators (operators that possess an orthonormal basis and a real valued spectrum). A quantitative criterion called veering index (VI) was developed in [BAL11] for estimating when veering occurs between different modes. These notions are an integral part of our mathematical toolset throughout this paper.

3. Contribution

In this work we consider the eigenbasis $\{\psi_i\}$ of a discrete step Hamiltonian operator of high potential energy like the one depicted

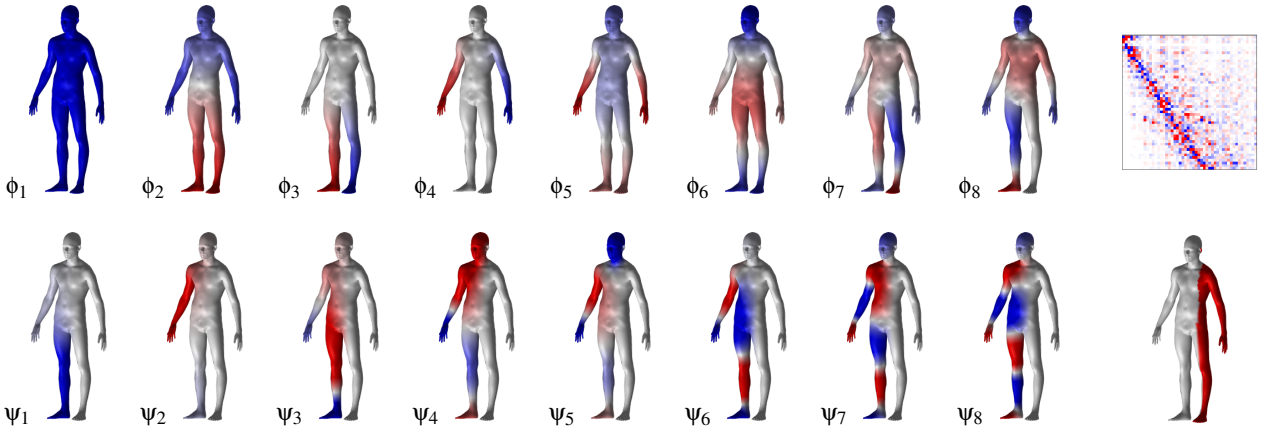

Figure 2: Top row: *The first few eigenfunctions of the Laplace-Beltrami operator.* Bottom row: *the first few Hamiltonian harmonics localized on the right side of the body with potential energy* $\tau = 5000$. *The high potential area is displayed in red on the bottom right shape. The relationship between eigenfunctions in the two bases is not evident as in the Neumann case, since eigenfunctions defined with Neumann boundary conditions are less deformed by partiality, being possibly different from zero on the boundary. To understand the relationship between the two eigenbases we can compute the functional map* $\mathbf{C} = \mathbf{\Phi}^{\top}\mathbf{A}\mathbf{\Psi}$, *where* $\mathbf{A}$ *is the mass matrix. The structure of* $\mathbf{C}$ *truncated to* $k = 50$ *is shown in the upper right matrix. Laplacian and Hamiltonian eigenfunctions are associated to rows and columns respectively. We notice a slanted diagonal similar to the one observed with Neumann functional maps [RCB*17].*

in Figure 2. We aim to study the relationship between this basis and the standard Laplace-Beltrami eigenbasis $\{\phi_i\}$. The functional map formalism is best suited to analyze this kind of relationship, and in this context we refer to the correspondence $\mathbf{C}$ between the two sets of eigenfunctions as a *Hamiltonian functional map*. The map $\mathbf{C}$ truncated to the first k harmonics localized on the low potential region, is equivalent to the functional map between the Laplacian on the full shape and the Dirichlet Laplacian on the partial shape (Figure 2, top right).

Experimentally, we observe that the *full* discrete map $\mathbf{C}$ (by full we mean that the matrix size is equal to the number of vertices on the mesh) exhibits a bi-diagonal structure determined by the potential energy (Figure 3) and its support region (Figure 4).

The focus of this paper is theoretical, aimed at understanding rigorously how Hamiltonian functional maps arise from potential variation in the discrete-geometric case. This investigation develops as following:

- In Section 4 we introduce the necessary background.
- In Section 5 we present the standard perturbative equations and use them to answer two questions:
  - How eigenvalues and eigenfunctions behave when the potential energy tends to infinity over a fixed region. In Section 5.1 we clarify this question through an original result (Theorem 3).
  - How eigenvalues and eigenfunctions interact when they are perturbed locally. This fact is explained in Section 5.2, where we adapt to our case existing results from structural engineering.
- In Section 6 we analyze the local interactions of Section 5.2 from a quantitative point of view, looking at concrete examples.
- Finally, in Section 7 we characterize the form of Hamiltonian functional maps combining the results of Sections 5.1 and 5.2. We will justify analytically the examples observed in Figures 3 and 4 with a construction based on the asymptotes of the eigenvalues.

In addition, we show in Section 8 how Hamiltonian functional maps are suited to tackle practical tasks in computer graphics by demonstrating state of the art results in the partial shape matching setting with a new algorithm, which exploits the natural relation between Dirichlet Laplacian and Hamiltonian eigenbases.

4. Background

We model a surface in the continuous setting as a 2-dimensional Riemannian manifold $\mathcal{M}$ with boundary $\partial\mathcal{M}$, equipped with the area element dx. The space of square integrable functions on $\mathcal{M}$ is denoted with $\mathcal{L}^2(\mathcal{M})$. The inner product on $\mathcal{L}^2(\mathcal{M})$ between two functions f and g is defined as

$$\langle f, g \rangle_{\mathcal{M}} = \int_{\mathcal{M}} f(x)g(x)dx\,. \tag{1}$$

4.1. Differential Operators

4.1.1. Laplacian

The first differential operator that we consider is the standard Laplace-Beltrami operator $\Delta_{\mathcal{M}}$. We recall that the manifold Laplacian is a self-adjoint operator. By the spectral theorem it admits a countable orthogonal basis $\{\phi_i\}$, obtained as the solution to the eigenvalue equation:

$$\Delta_{\mathcal{M}}\phi_i = \mu_i\phi_i\,. \tag{2}$$

The elements ϕ_i are the eigenfunctions of the Laplacian while μ_i are the associated real eigenvalues. We index the eigenvalues in non-decreasing order $\{0 \leq \mu_1 \leq \mu_2 \leq \dots\}$.

The behavior at the zeroth and first order of the eigenfunctions on $\partial\mathcal{M}$ depends on the chosen boundary conditions. Dirichlet conditions impose $\phi_i = 0$, while Neumann boundary conditions constraint the gradient of ϕ_i to be tangent to the boundary. In this paper, we assume Dirichlet conditions.

4.1.2. Hamiltonian

A Hamiltonian operator $H_{\mathcal{M}}$ can be obtained by adding to the Laplacian a projection operator P that depends on a potential function defined on the manifold. The simplest potential is a step function that places $\tau > 0$ energy density on a subset $\mathcal{N}$ of $\mathcal{M}$ and 0 on the complement $\overline{\mathcal{N}}$. Formally,

$$H_{\mathcal{M},\tau} = \Delta_{\mathcal{M}} + \tau P_{\mathcal{N}}\,, \tag{3}$$

with

$$P_{\mathcal{N}}(f)(x) = \begin{cases} f(x) & \text{if } x \in \mathcal{N} \\ 0 & \text{otherwise} \end{cases}\,. \tag{4}$$

Since $P_{\mathcal{N}}$ is self-adjoint, the resulting Hamiltonian is also self-adjoint and thus it admits a spectral decomposition:

$$H_{\mathcal{M},\tau}\psi_i = \lambda_i \psi_i\,. \tag{5}$$

As before, eigenvalues are ordered non-decreasingly $\{0 \leq \lambda_1 \leq \lambda_2 \leq \dots\}$. Any subsequent indexing of eigenvalues will use this ordering.

A fundamental result from quantum mechanics [Gri94] relates the Hamiltonian eigenfunctions to the Dirichlet eigenfunctions of the Laplacian computed on the complement of $\mathcal{N}$.

Theorem 1 *Let $H_{\mathcal{M},\tau}$ be a Hamiltonian operator (Eq. (3)). Its eigenfunctions ψ_i with energy $\lambda_i < \tau$, vanish for all $x \in \mathcal{N}$. It follows that $\phi_i = \psi_i$ where ϕ_i are the eigenfunctions of $\Delta_{\overline{\mathcal{N}}}$.*

4.2. Functional maps

Given two manifolds $\mathcal{M}$ and $\mathcal{N}$, a functional correspondence [OBCS*12] is modelled as the linear operator $T : \mathcal{L}^2(\mathcal{N}) \to \mathcal{L}^2(\mathcal{M})$ which, considering the orthonormal bases $\{\psi_j\}_{j\geq 1}$ and $\{\phi_i\}_{i\geq 1}$ acting respectively on $\mathcal{L}^2(\mathcal{M})$ and $\mathcal{L}^2(\mathcal{N})$, is defined as

$$Tf = \sum_{i,j} \langle \phi_i, f\rangle_{\mathcal{N}} \langle T\phi_i, \psi_j\rangle_{\mathcal{M}} \psi_j\,. \tag{6}$$

4.3. Discretization

In the discrete setting, $\mathcal{M}$ is approximated by a triangle mesh with n vertices $v_i \in V_{\text{int}} \cup V_{\text{bdr}}$, where each edge $e_{ij} \in E_{\text{int}} \cup E_{\text{bdr}}$ belongs to at most two triangle faces F_{ijk} and F_{jih}. We use the subscripts int and bdr on vertices and edges to denote interior and boundary, respectively. The discrete Laplace-Beltrami operator is defined in terms of two $n \times n$ matrices $\mathbf{W}$ and $\mathbf{A}$, where $\mathbf{A}$ is a diagonal matrix of local area elements a_i and $\mathbf{W}$ is a symmetric matrix of edge-wise

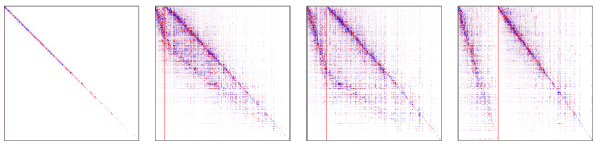

Figure 3: *Hamiltonian functional maps computed on the mesh in Figure 2 for the same potential at increasing values of τ. At convergence, the square matrix splits into two components (separated by a red line for visualization). In each component, a diagonal structure is visible. In Section 7 we show analytically how this structure arises when τ is increased.*

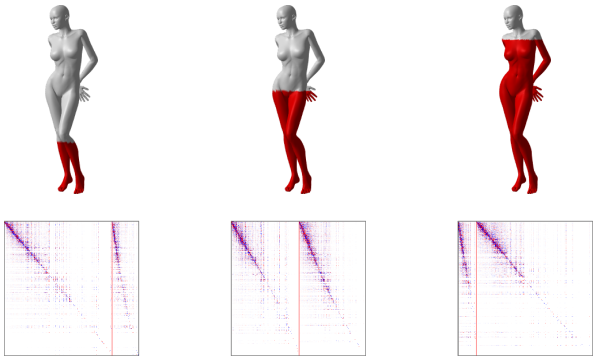

Figure 4: *Dependency of the structure of Hamiltonian functional maps with respect to the potential region. Experimentally, we observe that the width of the left component (separated by the red line) is proportional to the area of the low potential region.*

weights (also known as cotangent formula, see *e.g.* [MDSB03]):

$$w_{ij} = \begin{cases} -(\cot\alpha_{ij} + \cot\beta_{ij})/2 & e_{ij} \in E_{\text{int}} \\ 0 & (i \neq j) \wedge (i \in V_{\text{bdr}} \vee j \in V_{\text{bdr}}) \\ \sum_{k\neq i}(\cot\alpha_{ik} + \cot\beta_{ik})/2 & (i = j) \wedge v_i \in V_{\text{int}} \\ 1 & (i = j) \wedge v_i \in V_{\text{bdr}} \end{cases} \tag{7}$$

$$a_i = \begin{cases} \frac{1}{3}\sum_{jk:ijk\in F} A_{ijk} & v_i \in V_{\text{int}} \\ 0 & v_i \in V_{\text{bdr}} \end{cases} \tag{8}$$

where A_{ijk} is the area of triangle F_{ijk}. In the above formulas the Dirichlet boundary conditions are imposed accordingly. A generalized eigenproblem $\mathbf{W}\boldsymbol{\Phi} = \mathbf{A}\boldsymbol{\Phi}\text{diag}(\boldsymbol{\mu})$ is solved for computing a vector of the first k eigenvalues $\boldsymbol{\mu}$ and a matrix containing the first k eigenvectors $\boldsymbol{\Phi}$ as its columns.

The Hamiltonian is discretized as $\mathbf{H} = \mathbf{A}^{-1}\mathbf{W} + \tau\mathbf{P}$ with $\mathbf{P} = \text{diag}(\mathbf{v})$, where $\mathbf{v}$ is an n-dimensional 0-1 (indicator) vector that represents the step function. The generalized eigenproblem thus takes the form:

$$(\mathbf{W} + \tau\mathbf{A}\mathbf{P})\boldsymbol{\Psi} = \mathbf{A}\boldsymbol{\Psi}\text{diag}(\boldsymbol{\lambda})\,. \tag{9}$$

As above, we typeset with $\boldsymbol{\Psi}$ and $\boldsymbol{\lambda}$ the computed eigenquantities. The eigenfunctions are expressed in the hat basis. If it is required to

express an eigenfunction or any other function f in the Hamiltonian basis, the hat notation $\hat{f}$ will be used.

Functional maps in the discrete setting can be expressed as $n \times n$ matrices (possibly in a truncated basis of the first k eigenfunctions):

$$\mathbf{C}_{ij} = \langle T\phi_i, \psi_j \rangle_{\mathcal{M}} . \tag{10}$$

We consider a family of functional maps between the Hamiltonian basis on $\mathcal{M}$ and the Laplacian basis on $\mathcal{N} \subset \mathcal{M}$, parameterized by τ:

$$\mathbf{C}_{ij}(\tau) = \langle T\phi_i, \psi_j(\tau) \rangle_{\mathcal{M}} , \tag{11}$$

where $\psi_j(\tau)$ is the j-th eigenfunction of $H_{\mathcal{M},\tau}$. Examples of such maps are given in Figures 3 and 4.

5. Spectral analysis

In order to understand $\mathbf{C}(\tau)$ we focus on the evolution of the Hamiltonian spectral quantities with respect to τ. Their dynamic behavior influences the form of the functional map. We refer to this parametric study as *spectral tracking*.

The analysis develops first at a global scale and later focuses on the local interactions. We employ discrete equations given our setting. As we shall see, at a global scale this choice yields different results from the case in which the function space is infinite-dimensional. At a local scale instead, as proven in [PM86], the results hold both in the continuous and discrete case. A basic premise in our analysis is that the starting Laplacian spectrum is non degenerate, i.e. $\mu_i \neq \mu_j$ for all $i \neq j$.

The basic equations that describe the dynamic behavior of the analyzed eigensystem are stated.

Theorem 2 *Given a Hamiltonian matrix* $\mathbf{H} = \mathbf{A}^{-1}\mathbf{W} + \tau\mathbf{P}$*, the following holds:*

$$\frac{d}{d\tau}\lambda_i = \psi_i^\top \mathbf{A}\mathbf{P}\psi_i \tag{12}$$

$$\frac{d^2}{d\tau^2}\lambda_i = 2\sum_{j\neq i} \frac{(\psi_j^\top \mathbf{A}\mathbf{P}\psi_i)^2}{\lambda_i - \lambda_j} \tag{13}$$

$$\frac{d}{d\tau}\psi_i = \sum_{j\neq i} \frac{\psi_j^\top \mathbf{A}\mathbf{P}\psi_i}{\lambda_i - \lambda_j}\psi_j . \tag{14}$$

Proof See appendix A. □

Eqs. (12)-(14) are obtained by applying the standard perturbative derivatives [FK68] to our system.

Definition 1 *The inner product between eigenfunctions, weighted by the stiffness derivative, and computed as:*

$$\psi_j^\top \mathbf{A}\mathbf{P}\psi_i \tag{15}$$

is called modal coupling.

Modal coupling is present in each of the equations of Theorem 2 and it measures the influence between different eigenfunctions in a parametric eigensystem. In our case it is symmetric, since $\mathbf{AP}$ is a diagonal matrix, and since the weighted inner product is symmetric:

$$\psi_j^\top \mathbf{A}\mathbf{P}\psi_i = (\mathbf{P}\psi_i)^\top \mathbf{A}\psi_j = \psi_i^\top \mathbf{P}\mathbf{A}\psi_j = \psi_i^\top \mathbf{A}\mathbf{P}\psi_j . \tag{16}$$

We remark that Eq. (14) computes the derivative using the Hamiltonian basis. Interestingly, the Fourier coefficient with respect to ψ_i is zero, since it does not appear in the sum. The choice for this coefficient is not unique as noted in [Nel76]: eigenvectors are invariant to scale, so the set of all possible derivatives is a 1-dimensional affine space. Setting it to zero in a symmetric eigensystem imposes the orthonormality constraint on the basis across the evolution with respect to τ.

5.1. Global analysis

Figure 5 plots the first eigenvalues of the Hamiltonian on the human shape illustrated in Figure 2 as functions of τ. It can be observed that each eigenvalue curve, called *eigenvalue loci*, grows as τ is increased. This fact can be easily proven:

Proposition 1 *Consider* $\mathbf{H}_1 = \mathbf{A}^{-1}\mathbf{W} + \tau_1\mathbf{P}$ *and* $\mathbf{H}_2 = \mathbf{A}^{-1}\mathbf{W} + \tau_2\mathbf{P}$ *with* $\tau_1 \leq \tau_2$*. Let* λ_{i1} *and* λ_{i2} *be the i-th eigenvalues of* $\mathbf{H}_1$ *and* $\mathbf{H}_2$*, respectively. Then* $\lambda_{i1} \leq \lambda_{i2}$*.*

Proof See Appendix A. □

Observing the left plot in Figure 5 we notice a structural asymptotic behavior. The eigenvalue loci seem to stabilize after τ has been fairly increased. They do not stabilize gently, but undergo a sequence of local bumps, forming patterns that sometimes are clearly visible, resembling braids. The braids seem to move with constant first derivative. The following result explains what happens after all local interactions have ended.

Theorem 3 *Let* $\mathbf{H} = \mathbf{A}^{-1}\mathbf{W} + \tau\mathbf{P}$ *be a Hamiltonian matrix such that r components* $\mathbf{P}_{k_0,k_0}$ *of the diagonal of* $\mathbf{P}$ *are equal to zero and* $n - r$ *components* $\mathbf{P}_{k_1,k_1}$ *are equal to one. By indexing with i the first r eigenvalues and with j the subsequent ones, we get:*

$$\lim_{\tau\to+\infty} \lambda_i \in [\mu_1, \mu_n] , \tag{17a}$$

$$\lim_{\tau\to+\infty} \frac{d}{d\tau}\lambda_i = 0 , \tag{17b}$$

$$\lim_{\tau\to+\infty} \psi_{ik_1} = 0 , \tag{17c}$$

$$\lim_{\tau\to+\infty} \lambda_j = +\infty , \tag{17d}$$

$$\lim_{\tau\to+\infty} \frac{d}{d\tau}\lambda_j = 1 , \tag{17e}$$

$$\lim_{\tau\to+\infty} \psi_{jk_0} = 0 . \tag{17f}$$

Proof See Appendix A. The reader is warmly advised to read the proof since it is an interesting application of the "eigenvectors from eigenvalues" formula, recently rediscovered in [DPTZ19]. □

Eigenvalue asymptotics

Eqs. (17d) and (17a) tell us that the r lowest eigenvalues will stabilize to a finite value (not greater than the maximum Laplacian eigenvalue) while the other $n - r$ will grow indefinitely. The rate of growth is governed by Eqs. (17b) and (17e): the lowest eigenvalues have horizontal asymptotes while the highest have oblique asymptotic (with a slope equal to 1). This behavior is expected from the fact that for large τ, the diagonal component of the Hamiltonian dominates the Laplacian component. The local interactions originate for the same reason: an eigenvalue with low index may have

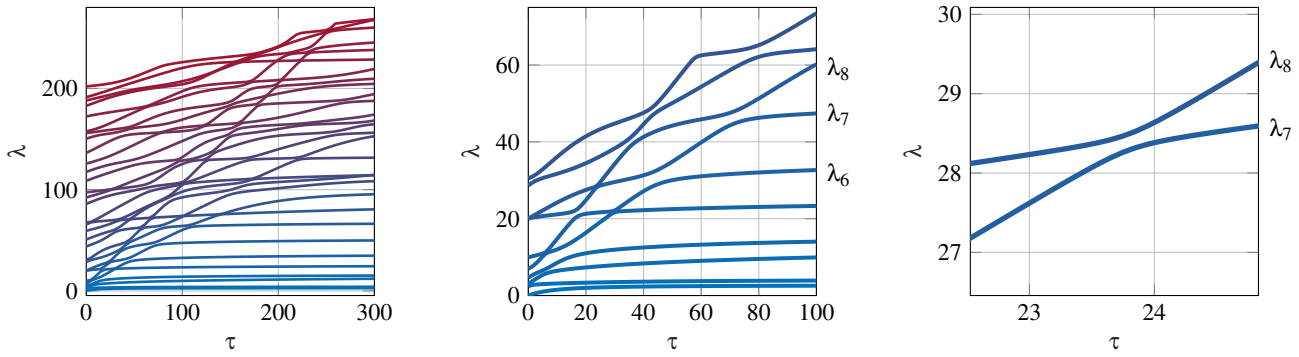

Figure 5: Left: *The first 30 eigenvalue curves (loci) computed on the mesh of Figure 2. The potential energy* τ *is varied from 0 to 300 by increments of* $\delta\tau = 1$. *For each* τ *the eigenvalues are plotted along the vertical axis, interpolating the discrete points. Higher indexed curves are colored red while lower indexed curves are colored blue. At a global scale, "braid" patterns can be observed; some of them are more evident, growing in parallel over the diagonal of the axis. Differently, lower eigenvalue curves tend to stabilize near a constant value.* Center: *Restriction to the first 10 eigenvalues of the left plot for* $\tau \in [0, 100]$. *At certain values of* τ *some eigenvalue curves seem to intersect, for example, the seventh and eight curves (from the bottom) around* $\tau = 24$. Right: *The intersection is only apparent, since increasing the resolution we observe a veering interaction. For other values of* τ *in the central plot, curves veer "at a distance" , for example eigenvalues* λ_6 *and* λ_7 *near* $\tau = 16$. *In both cases, there seems to be an exchange in first derivative between proximal curves.*

a high derivative at the start, but in the end its derivative must stabilize at 0. Meanwhile it "bounces" on proximal curves, losing or gaining velocity at each interaction (this will be formalized better in the next Subsection). The derivative information transfers to higher indexed eigenvalues escaping from the interacting phase with a value approximately equal to 1.

Eigenfunction asymptotics

Eqs. (17c) and (17f) explain formally the well known localization property of the eigenfunctions. As expected from Theorem 1, the lower indexed eigenfunctions localize on the low potential region $\overline{\mathcal{N}}$, since the components associated to the high potential area $\mathcal{N}$ tend to zero.

However, differently from the continuous setting, the *higher indexed* eigenfunctions localize on the *high potential* area. At the limit, the eigenfunctions span two orthogonal eigenspaces $\mathrm{Ker}(\mathbf{P})$ and $\mathrm{Ker}(\mathbf{P})_\perp$. We show in Figure 1 this complementary localization on the body and the head of the elephant.

This analysis is valid for the discrete setting, but the continuous setting can be recovered by replacing the finite eigenvectors ψ_i, ψ_j and the finite matrices with infinite counterparts. The main difference is that, in the continuous setting, the local interactions keep going on indefinitely so *each* eigenvalue must stabilize at a finite value, with derivative equal to zero. Consequently, for each τ, an eigenfunction that stabilizes on the high potential area cannot exist as in the discrete case.

5.2. Local analysis

We now concentrate on the local interactions that we observe in Figure 5. These types of interactions are not specific to the Hamiltonian case, and can be encountered in a wide range of parametric eigensystems. Given their generality there exists a wide literature, especially in engineering, that studies the topic. We draw on this literature, especially on [PM86] and [BAL11]. The local behavior of generalized Hermitian eigensystems like ours stems from the results in Theorem 2. These equations, however, are too complex to use directly given the summations in Eqs. (13) and (14), therefore useful approximations are employed.

Eigenvalue interactions

Let us begin with the interactions between eigenvalues. Suppose that at a certain point $\tau_0 > 0$, two eigenvalues λ_i and λ_j are such that $|\lambda_i - \lambda_j| = \min_{k \neq l} |\lambda_k - \lambda_l|$. It is clear that i and j must be consecutive numbers since other pairs do not minimize the difference. W.l.o.g. let $j = i + 1$. Using Eq. (13), the second order derivative can be approximated with:

$$\frac{d^2}{d\tau^2}\lambda_i \approx 2\frac{(\psi_j^\top \mathbf{A}\mathbf{P}\psi_i)^2}{\lambda_i - \lambda_j}, \tag{18}$$

$$\frac{d^2}{d\tau^2}\lambda_j \approx 2\frac{(\psi_i^\top \mathbf{A}\mathbf{P}\psi_j)^2}{\lambda_j - \lambda_i}. \tag{19}$$

The estimation holds because the differences between the other eigenvalue pairs have a small influence on the total derivative.

Comparing Eqs. (18) and (19) and using Eq. (16), it can be noticed that the approximations of the second eigenvalue derivatives have the same absolute value and different signs (given by the inverted denominators). Under the assumption that the modal couplings are different from zero, this translates into opposite curvatures of the respective loci during the interaction. This means that the two curves repel one another with an intensity proportional to their distance. We will refer to this kind of interactions between eigenvalues as *veering interactions*. In the ideal case where the approximations become equalities, we will talk about *ideal veering interactions*.

Given the symmetry of the interaction, the first derivatives are exchanged when veering ends. This explains the progressive loss of first derivative of a loci at a global scale. In a general setting, modal couplings could be zero and non parallel loci would cross.

Eigenfunction interactions

We now consider the eigenfunctions and study how they transform while the associated eigenvalues perform a veering interaction. Let ψ_i^0 and ψ_j^0 be two eigenfunctions of $\mathbf{H} = \mathbf{A}^{-1}\mathbf{W} + \tau_0\mathbf{P}$ with associated eigenvalues λ_i^0 and λ_j^0 ($j = i+1$). Consider that $\tau_0 \in [\tau_1, \tau_2]$, an interval over which an ideal veering interaction occurs between λ_i and λ_j.

As in the previous case, $\frac{1}{\lambda_i^0 - \lambda_k^0} \approx 0$ for $k \neq j$ and $\frac{1}{\lambda_j^0 - \lambda_k^0} \approx 0$ for $k \neq i$ in $[\tau_1, \tau_2]$. The vector representation of the functional derivatives (Eq. 14) can be approximated in the Hamiltonian basis as:

$$\widehat{\frac{d}{d\tau}\psi_i^0} \approx \begin{bmatrix} 0 & \dots & 0 & \frac{\psi_j^{0\top}\mathbf{A}\mathbf{P}\psi_i^0}{\lambda_i^0 - \lambda_j^0} & \dots & 0 \end{bmatrix}^\top \tag{20}$$

$$\widehat{\frac{d}{d\tau}\psi_j^0} \approx \begin{bmatrix} 0 & \dots & \frac{\psi_i^{0\top}\mathbf{A}\mathbf{P}\psi_j^0}{\lambda_j^0 - \lambda_i^0} & 0 & \dots & 0 \end{bmatrix}^\top, \tag{21}$$

where the nonzero components in $\frac{d}{d\tau}\psi_i$ and the $\frac{d}{d\tau}\psi_j$ are only the j-th and i-th, respectively (notice the inversion).

These two vectors lie on the 2-dimensional subspace Γ spanned by the basis vectors ψ_i^0 and ψ_j^0. By differentiating Eqs. (20) and (21) with respect to τ repeatedly, higher order derivatives are obtained. Since differentiating the null components we obtain zeros, these higher order derivatives have only the j-th or i-th components different from zero, like the first derivatives, so they still belong to Γ. Now for all $\tau \in [\tau_1, \tau_2]$ we can compute ψ_i and ψ_j with a Taylor expansion in τ_0. The Taylor expansion is an infinite linear combination of vectors in Γ, so $\psi_i, \psi_j \in \Gamma$ for all $\tau \in [\tau_1, \tau_2]$. This means that during an ideal veering interaction, the two eigenfunctions will interact only with each other and transform on a constant 2-dimensional subspace.

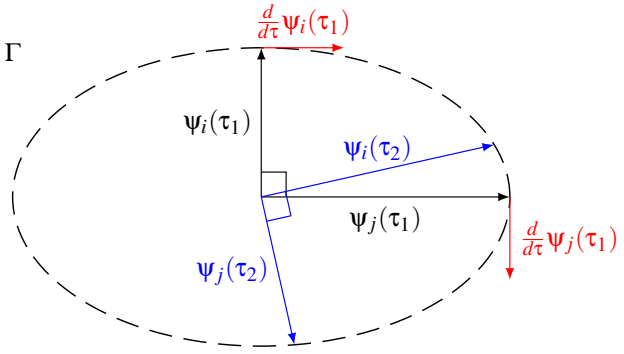

Figure 6: *Geometric interpretation of eigenfunctions rotating on Γ. Since the mass matrix $\mathbf{A}$ is a symmetric matrix, all eigenvectors of $\mathbf{A}$-norm equal to 1 must lie on an ellipse. The interacting Hamiltonian eigenfunctions ψ_i and ψ_j are rotated by the derivatives $\frac{d}{d\tau}\psi_i$ and $\frac{d}{d\tau}\psi_j$. At the end of the interaction $\psi_i(\tau_1)$ has transformed into $\psi_i(\tau_2)$, an eigenvector near the eigenspace spanned by $\psi_j(\tau_1)$; $\psi_j(\tau_1)$ transforms into $\psi_j(\tau_2)$, an eigenvector close to $\psi_i(\tau_1)$. An approximate exchange is performed at the end of the interaction in the ideal case. Notice that $\psi_i(\tau_2)$ keeps the sign of $\psi_j(\tau_1)$ while $\psi_j(\tau_2)$ inverts it. The same effect can be observed in Figures 8 and 9.*

From Eqs. (20) and (21) (omitting the indexing since the same formulas hold for each $\tau \in [\tau_1, \tau_2]$) we can write:

$$\frac{d}{d\tau}\psi_i \approx \frac{\psi_j^\top \top \mathbf{A}\mathbf{P}\psi_i}{\lambda_i - \lambda_j}\psi_j, \tag{22}$$

$$\frac{d}{d\tau}\psi_j \approx \frac{\psi_i^\top \mathbf{A}\mathbf{P}\psi_j}{\lambda_j - \lambda_i}\psi_i = -\frac{\psi_j^\top \mathbf{A}\mathbf{P}\psi_i}{\lambda_i - \lambda_j}\psi_i. \tag{23}$$

Let us assume w.l.o.g. that $\psi_j^\top \mathbf{A}\mathbf{P}\psi_i > 0$. The approximated derivatives have the following properties:

- They are orthogonal

$$\left(\frac{d}{d\tau}\psi_j\right)^\top \mathbf{A}\frac{d}{d\tau}\psi_i = -\left(\frac{\psi_j^\top \mathbf{A}\mathbf{P}\psi_i}{\lambda_i - \lambda_j}\right)^2 \psi_j^\top \mathbf{A}\psi_i = 0. \tag{24}$$

- They have the same norm

$$\left\|\frac{d}{d\tau}\psi_i\right\| = \left\|\frac{d}{d\tau}\psi_j\right\| = \left|\frac{\psi_j^\top \mathbf{A}\mathbf{P}\psi_i}{\lambda_i - \lambda_j}\right|. \tag{25}$$

- $\frac{d}{d\tau}\psi_i$ has same direction and orientation as ψ_j.
- $\frac{d}{d\tau}\psi_j$ has the same direction as ψ_i but opposite orientation.

A dynamical system that satisfies these conditions is a rotation with variable angular speed (see Figure 6). The angular velocity is directly proportional to the common norm of the derivatives. It takes into account the modal coupling $|\psi_j^\top \mathbf{A}\mathbf{P}\psi_i|$ and the difference between associated eigenvalues $|\lambda_j - \lambda_i|$. It follows that the rotation has a higher intensity were both $\frac{1}{|\lambda_j - \lambda_i|}$ and the modal coupling are highest. It is easy to see that $\frac{1}{|\lambda_i - \lambda_j|}$ achieves its highest value at the point τ^* where the eigenvalue loci have maximum curvature, because $|\lambda_i - \lambda_j|$ is smallest.

Interestingly, [BAL11] showed that the modal coupling is also maximized at the same point τ^*. Additionally, they proved that in the ideal veering interaction a rotation about $\pi/2$ is performed, where an angle of $\pi/4$ is swept when $\tau = \tau^*$. This means that at the end of the rotation, eigenfunctions are exchanged: if at the beginning of the rotation λ_i and λ_j are the eigenvalues associated to $\psi_i(\tau_1)$ and $\psi_j(\tau_1)$, respectively, at its end they will be associated to $\psi_i(\tau_2) \approx \psi_j(\tau_1)$ and $\psi_j(\tau_2) \approx \psi_i(\tau_1)$. More generally, after a non-ideal interaction, $\psi_i(\tau_2)$ ($\psi_j(\tau_2)$) will be a linear combination of $\psi_i(\tau_1)$ and $\psi_j(\tau_1)$, weighted accordingly. In the case in which modal dependency with more distanced modes is present, the linear combination would include contributions of other eigenvectors. Figure 6 illustrates eigenvector interactions abstractly. In the following section we will look at some concrete example after we quantify the interactions.

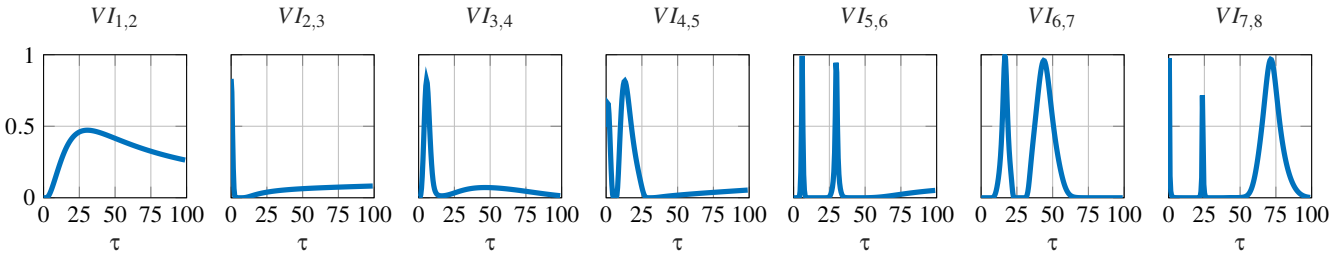

Figure 7: *Veering indices ($VI_{i,j}$) computed for the Hamiltonian eigenfunctions in Figure 2 with $\delta\tau = 0.5$ and an approximating factor $k = 25$. The plots are consistent with loci behavior since a bump appears where a veering interaction occurs in Figure 5. Some indices like $VI_{1,2}$ do not peak very much but spread across a large area, indicating a blurry transformation between eigenfunctions. Other indices like $VI_{5,6}$ and $VI_{6,7}$ have very high peaks in small neighborhoods of the parameter.*

6. Veering index

Observing the local interactions of the eigenfunctions is useful to understand the way in which Hamiltonian functional maps evolve at small variations of τ. Until now we have focused on the general theoretical setting analyzing ideal interactions, but we still do not have a tool to quantify the occurrence of spectral interactions in real cases. To this end, we employ a metric developed in [BAL11] that can be used to quantify objectively veering interactions, or equivalently interactions between eigenfunctions.

Definition 2 *The veering index between two Hamiltonian eigenpairs of index i and j is defined as:*

$$VI_{i,j} = MDF_{i,j} \times CSQ_{i,j} \times MDF_{j,i} \tag{26}$$

where:

$$CSQ_{i,j} = \frac{(\psi_j^\top \mathbf{A}\mathbf{P}\psi_i)^2}{(\psi_j^\top \mathbf{A}\mathbf{P}\psi_i)^2 + (\psi_i^\top \mathbf{A}\mathbf{P}\psi_i - \psi_j^\top \mathbf{A}\mathbf{P}\psi_j)^2} \tag{27}$$

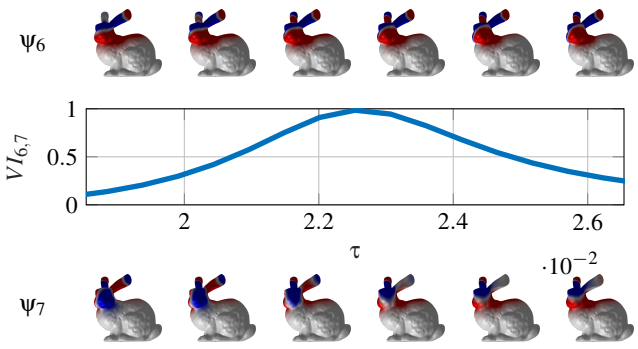

Figure 8: *Eigenfunctions exchanging on the bunny. The interaction takes place between $\tau_1 = 0.018$ and $\tau_2 = 0.027$ and involves ψ_6 and ψ_7. After the interaction has settled, we obtain $\psi_6(\tau_2) \approx -\psi_7(\tau_1)$ (top right) and $\psi_7(\tau_2) \approx \psi_6(\tau_1)$ (bottom right). The veering index is plotted between the two sequences. It peaks near $\tau = 0.023$, where most of the rotation takes place. Where $VI_{6,7} < 0.8$ no major changes occur.*

$$MDF_{i,j} = \frac{\frac{\psi_j^\top \mathbf{A}\mathbf{P}\psi_i}{\lambda_i - \lambda_j}}{\sum_{k \neq i} \frac{\psi_k^\top \mathbf{A}\mathbf{P}\psi_i}{\lambda_i - \lambda_k}}. \tag{28}$$

We refer the reader to [BAL11] for an in-depth understanding of this metric. It suffices to know that it combines two types of factors in order to give a natural measurement of the veering interaction between two modes. The first factor is the cross-sensitivity quotient $CSQ_{i,j}$. It measures the intensity of veering between modes i and j as a quotient between the current modal coupling and the maximum coupling in τ^*. The modal dependence factors $MDF_{i,j}$ and $MDF_{j,i}$ are the quotients between the Fourier coefficients that appear in Eqs. (20) and (21) and the sum between all the coefficients of the eigenfunctions derivatives (Eq. (14)). They measure how much the approximations in Eqs. (20) and (21) hold, attaining maximum value if the rotation between the eigenvectors takes place on Γ. Since both factors are real values between 0 and 1, the veering index has the same range.

The veering indices $VI_{i,i+1}$ for the Hamiltonian computed on the human shape in Figure 2 are plotted in Figure 7. Higher distanced indices $V_{i,i+d}$ with $d = 2,3,4$ have been calculated as well but they were always lower than 0.1. The same has been observed in other experiments, meaning that proximal interactions are most frequently encountered. In order to obtain the modal dependence factors, we have approximated the denominators (the sum of the coefficients in Eq. (14)) with a sum over the first k modes. An alternative approach is given by Nelson's method [Nel76] that computes the derivative coefficients by solving a linear system. We have preferred the choice of the approximations since they are easier to compute and accurate enough even for small values of k.

A legitimate question that one could ask is how an eigenfunction ψ_i transforms when it does not interact with other eigenfunctions, that is when $VI_{i,k} \approx 0$ for each k. The veering index is zero when one of the two factors $CSQ_{i,k}$ and $MDF_{i,k}$ ($MDF_{k,i}$) is zero. Both happen to be null when the modal couplings $\psi_k^\top \mathbf{A}\mathbf{P}\psi_i$ are null. Using this information in conjunction with Eq. (14) we notice that the derivative is zero in those phases, so the eigenfunction does not change. In practice, the index could have a small value while being

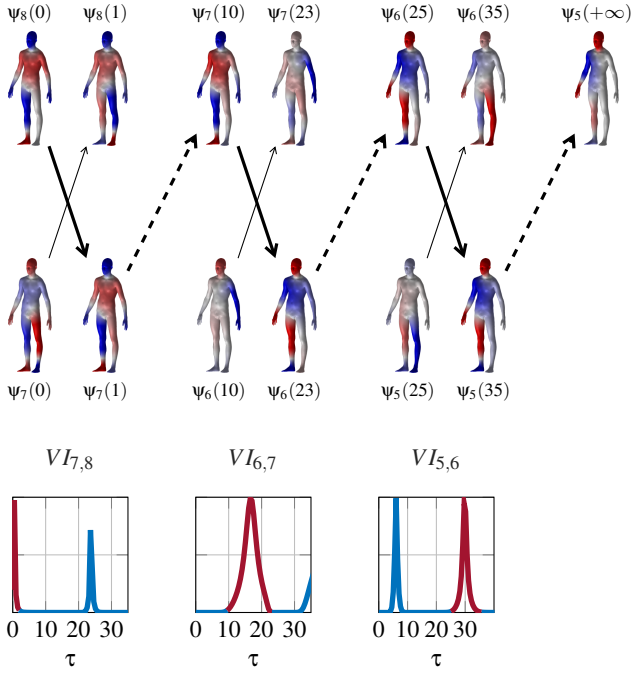

Figure 9: *Tracking of the Laplacian eigenfunction* $\phi_8 = \psi_8(0)$ *from Figure 2. An exchange in sign is present (as seen in Figure 6) in the second interaction.* Top row: *Evolution path of the eigenfunction on the surface, at increasing values of* τ. Bottom row: *Corresponding veering indices that were used to spot the interactions.*

different from zero, so the eigenfunction could still change with low intensity.

Armed with the veering index we can easily spot when eigenfunctions perform good exchanges, because this happens at values of τ where $VI \approx 1$. An example is given in Figure 8, where we show the evolution of two such eigenfunctions on the bunny model.

Eigenfunction tracking

A first approach to understanding how Hamiltonian functional maps evolve, is the tracking of individual eigenfunctions by following the peaks of the veering index. Starting from the observation that the Hamiltonian at $\tau = 0$ corresponds to the Laplacian, we fix an eigenfunction $\phi_i = \psi_i(0)$. The idea is to look for the first τ where $VI_{i,i+1} \approx 1$ (or $VI_{i-1,i} \approx 1$). After the interaction, a significant part of ψ_i (depending on the interaction strength), is transferred to ψ_{i+1} (or equivalently ψ_{i-1}) and becomes associated with λ_{i+1} (or λ_{i-1}). This procedure is repeated until the last eigenvalue λ_l associated with the tracked function stabilizes. The tracked eigenfunction seems to follow a path between exchanging eigenvalue loci. On the functional map $\mathbf{C}$, the i-th row associated to the eigenfunction ϕ_i should peak at the index l, associated to λ_l. For Laplacian eigenfunctions with low indices, there are typically a small number of total interactions and are easier to track.

In Figure 9 we depict the tracking process starting from the eighth eigenfunction of the example in Figure 2, following the indices computed in Figure 7, reported on the bottom row. Each of the three interactions is represented by two crossing arrows that show the exchange between eigenfunctions before and after veering. The tracking path of ϕ_8 is highlighted by the thick arrows: the contiguous lines shows the exchange of the tracked eigenfunction with an eigenfunction of a proximal eigenvalue curve, while the dashed lines indicate that the function remains relatively constant on intervals over which the veering index is approximately 0. In summary, the component on the low potential area of ϕ_8 transfers to ψ_5 at infinity.

7. Hamiltonian functional maps

In this Section we combine the asymptotic information of Theorem 3 with the local behavior investigated in Section 5.2 in order to give a comprehensive description of the Hamiltonian functional maps. We mainly seek to characterize the bi-diagonal form of the maps.

7.1. Optimal exchange case

We first put ourselves in the *ideal* setting where all veering interactions exchange eigenfunctions optimally ($VI = 1$). The asymptotes of the eigenvalue curves play a central role in this Section, so we begin with the following definition.

Definition 3 *The i-th support line* σ_i *of a Hamiltonian matrix* $\mathbf{H}$ *is the asymptote (whose existence is guaranteed by Theorem 3) of its i-th eigenvalue curve* λ_i. *Let*

$$d(\sigma_i) = \lim_{\tau \to +\infty} \frac{d}{d\tau} \lambda_i \in \{0, 1\}. \tag{29}$$

σ_i *is called an oblique support if* $d(\sigma_i) = 1$, *while if* $d(\sigma_i) = 0$ *it is called a horizontal support. The ordered sequence of support lines will be denoted with* Σ. *We can label* Σ *with the sequence of derivatives:*

$$c = d(\sigma_1), \ldots, d(\sigma_n). \tag{30}$$

Support lines are a useful concept, because they guide the real eigenvalue curves in the ideal case. To see why this happens, consider the eigenvalue curve λ_i whose asymptote is σ_i. W.l.o.g. suppose that σ_i is an oblique support. This line can either intersect a horizontal support, or not. In the former case, let us consider the crossing at the largest τ, denoting with σ_j the intersecting horizontal support. At that point, the associated eigenvalue curves λ_i and λ_j undergo an optimal veering interaction. As argued in Section 5.2, their first derivative exchanges during the interaction. This means that at the corresponding τ where the interaction begins, λ_i will be associated with σ_j and λ_j with σ_i. Applying the same reasoning to all the other intersections between σ_i and the horizontal supports for $\tau \to 0$, we observe that different eigenvalue curves "snap" to σ_i. If σ_i does not intersect other horizontal supports, we have $\lambda_i = \sigma_i$ since no modal interactions happen. The behavior we described justifies the support nature of the asymptotes.

Interestingly, eigenvalue curves would become support lines if modal interactions are constantly equal to 0, since by Eq. (13) all second derivatives would cancel out and all veering interactions would turn to crossing interactions (at the intersections between

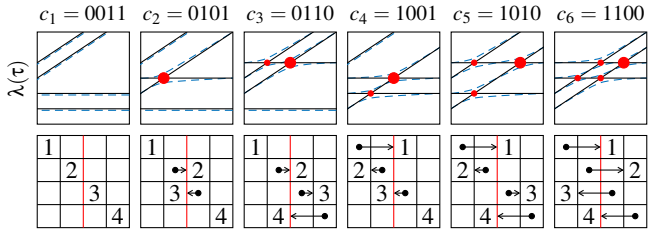

Figure 10: Top: *All possible crossing configurations in the* 4×4 *case with 2 oblique supports and 2 horizontal supports. Support lines are plotted in black, while the underlying eigenvalue curves are dashed. The crossings are displayed in red and the thicker dot is* γ^*. Bottom: *Ideal functional maps associated to each configuration. For* $\tau = 0$ *we have the identity. For* $\tau = +\infty$ *the maps change according to the flow of the eigenfunctions along support lines.*

support lines). This configuration arises in the ideal non-geometric case where the Laplacian degenerates to a diagonal matrix, whose eigenvalues are simply the components of the diagonal. The behavior of such system is equivalent to the one that we are investigating here, since a perfect veering interaction is equivalent to a crossing interaction with respect to the eigenfunction exchange. We stress the importance of this equivalence since it will be useful in the following Subsection, where we will pass to the real case.

A support line is associated to a single eigenfunction for all τ. In some sense, the eigenfunction "flows" along it. This happens because at each crossing, the underlying eigenvalue curves exchange optimally their eigenfunctions.

Let us now consider all possible ways in which support lines can cross.

Proposition 2 *Let* Σ *be a sequence of support lines and* $\mathcal{C}$ *the set of all their intersections. If* γ_1 *is the intersection between* $\sigma_{i_{11}}$ *and* $\sigma_{i_{12}}$ *and* γ_2 *is the intersection between* $\sigma_{i_{21}}$ *and* $\sigma_{i_{22}}$*, we set*

$$\gamma_1 \leq \gamma_2 \iff |i_{11} - i_{12}| \leq |i_{21} - i_{22}|. \tag{31}$$

Then $\langle \mathcal{C}, \leq \rangle$ *is a preorder with a maximum* γ^*.

The possible arrangements of crossings, which form ordered structures, are determined only by the order in which support lines of different slopes meet. We show an example of possible configurations in Figure 10. It is clear that γ^* is the intersection between the most distanced pair of intersecting horizontal-oblique support lines.

Ideal Hamiltonian maps

Now we show how an ideal Hamiltonian functional map takes form as $\tau \to +\infty$. In order to have a clear understanding of what is going on, we encourage the reader to accompany the reading of the following lines with the diagram presented in Figure 11, which provides a visual proof of the phenomenon.

Let Σ be a support sequence labeled by c. We can write $c = c_0 c_m c_1$ where c_0 contains only zeros with $|c_0| = n_0$, c_1 contains only ones, with $|c_1| = n_1$ and c_m is such that $c_{m_1} = 1$ and

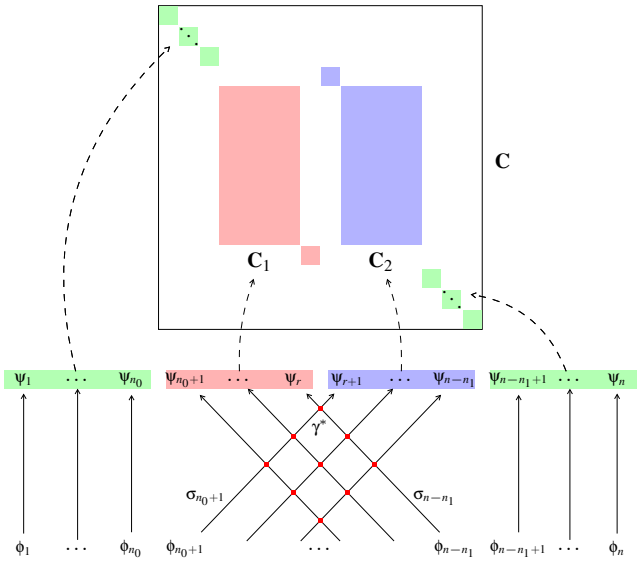

Figure 11: *Representation of the ideal Hamiltonian functional map structure. Support lines are represented as arrows between the eigenfunctions of the Laplacian basis and of the Hamiltonian basis. There are four groups: the first group on the left (green matches) contains the horizontal supports associated with* c_0 *so they match the eigenfunctions directly. The second group are oblique supports that cross horizontal supports (blue matches). The third group are horizontal supports that cross oblique supports (red matches). Finally, the fourth group are the oblique supports associated to* c_1 *(green matches). For illustration convenience we put all supports of the third group after the first group, but in general they are interleaved (reference Figure 10). In order to know where the row index of a Laplacian eigenfunction will match with the column index of a Hamiltonian eigenfunction, one only needs to follow the relative support line. These matches are displayed in the resulting ideal functional map* $\mathbf{C}$*. We explicitly depict the trivial green correspondences, the matches between* ϕ_{n_0+1} *and* ψ_{r+1} *(red square) and the match between* ϕ_{n-n_1} *and* ψ_r *(blue square). The* $\mathbf{C}_1$ *and* $\mathbf{C}_2$ *components are such that on each row of* $\mathbf{C}$ *the matched column index belongs to one of them but not to both (differently from the real case, as we shall see). This results in the bi-diagonal structure that we observe in Figures 3 and 4, where all the off-diagonal sparsity is cancelled. The dependence on the region of the potential is clear, since the map is divided in the left component of* r *columns (associated to zero potential region) and in the right component of* $n - r$ *columns (associated to the high potential region).*

$c_{m_{n-n_0-n_1}} = 0$. The support lines labeled by c_0 and c_1 are parallel so no intersections occur between them, thus we can focus only on Σ_m labeled by c_m.

The maximum crossing γ^* is the intersection between σ_{n_0+1} and σ_{n_1-1}, the first and the last support line in Σ_m. Since σ_{n_0+1} is the first oblique support line, and since there are r horizontal support lines, it must send ϕ_{n_0+1} into ψ_{r+1} and ϕ_{n_0+1} in ψ_{r+1} (the reader can follow the corresponding arrow in Figure 11).

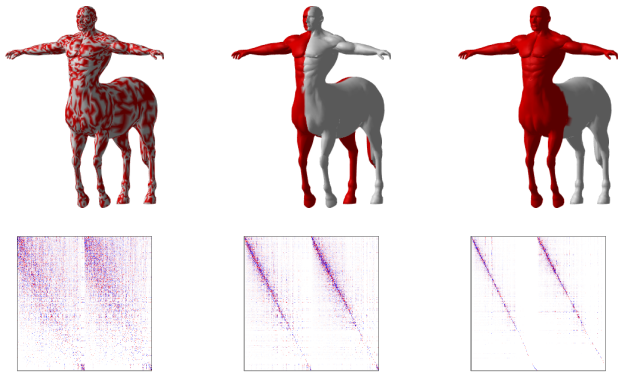

Figure 12: *Random potentials (left) are associated to dispersed functional maps. Sharper diagonals are related to regular potentials. The cut region affects the dispersion (compare center to right) as in the Neumann case [RCB*17]. Off-diagonal dispersion is dominant in the upper part of each diagonal. The lower part of the diagonals tend to be less dispersed because of the localization property of higher frequency Laplacian eigenfunctions [CH15].*

Consider ψ_i, ψ_j with $n_0 + 1 < i < j < r$. It is clear that $\psi_i = \phi_k$ and $\psi_j = \phi_l$ with $k < l$. The same is valid for $r+1 < i < j < n - n_1$. This results in two slanted diagonals $\mathbf{C}_1$ and $\mathbf{C}_2$.

7.2. Real exchange case

Now let us tackle the general case in which spectral interactions are not optimal. We can write a Laplacian matrix as $\mathbf{L} = \mathbf{L}_d + \mathbf{L}_o$, where $\mathbf{L}_d = \mathrm{diag}(\mathbf{L})$ and $\mathbf{L}_o = \mathbf{L} - \mathbf{L}_d$ is the off-diagonal component. The Hamiltonian is decomposed in the following way:

$$\mathbf{H} = \mathbf{L} + \tau\mathbf{P} = \mathbf{L}_d + \mathbf{L}_o + \tau\mathbf{P} = (\mathbf{L}_d + \tau\mathbf{P}) + \mathbf{L}_o \,. \tag{32}$$

$\mathbf{H}$ is the sum between the matrix $\mathbf{L}_d + \tau\mathbf{P}$, whose loci coincide with the intersecting support lines (since it corresponds to the degenerate crossing configuration being diagonal, as explained in the previous Subsection), and by a *constant* matrix $\mathbf{L}_o$, which encodes the edge information on the mesh. By applying Weyl's inequality (Lemma 1, Appendix A) each eigenvalue λ_i of $\mathbf{H}$ is bounded by the sum between the i-th *ideal* eigenvalue δ_i of $\mathbf{L}_d + \tau\mathbf{P}$ and the extremal eigenvalues $\omega_{\min}$ and $\omega_{\max}$ of $\mathbf{L}_o$ [†] (constant for each τ):

$$\delta_i + \omega_{\min} \leq \lambda_i \leq \delta_i + \omega_{\max} \,. \tag{33}$$

Being the real eigenvalues bounded to the ideal eigenvalues, the latter will follow the former with the difference that crossing interactions will be replaced by veering interactions, which in general are non optimal. Consequently, real Hamiltonian functional maps follow the structure of the maps in Figure 11, with the difference that components of an initial eigenfunction will separate on more than one eigenvalue curve (depending on VI at each interaction), resulting in the spreading pattern of the map. Experimental evidence suggests that random, dispersed potentials, result in functional maps that are fairly spread, as shown in Figure 12.

[†] It follows that the eigenvalues λ_i are bound by spectral norm $||\mathbf{L}_o||_2$. This bound can be enlarged to $||\mathbf{L}_o||_1$. Since $||\mathbf{L}_o||_1$ is equal to the maximum sum (in absolute value) over the columns of $\mathbf{L}_o$, the perturbation with respect to the ideal case depends on geometric information (e.g. the maximum degree of a vertex). We leave this investigation for future studies.

8. Applications

The theoretical analysis performed in the previous sections provides a formal framework to understand the parametric family of Hamiltonian functional maps. Although the Hamiltonian spectrum has been employed previously in the geometry processing community, to our knowledge explicit Hamiltonian functional maps have not been considered in any geometry processing task before. In the current Section, we show the practical utility of this formalism to tackle problems in computer graphics. We present a direct application in the context of partial shape matching, for which we obtain state of the art results. For this task we advocate for the use of Hamiltonian functional maps to provide a framework which fits in a natural way to previously existing pipelines.

As stated in the introductory section, partial shape matching deals with the problem of finding a correspondence between a deformable shape and a possible deformed subset of it. We set ourselves in the (nearly) isometric setting. State of the art results are those of [RCB*17], where the framework of [OBCS*12] for finding a correspondence in the spectral domain of the Laplace-Beltrami operator is lifted to the partial setting. More recently in [RTO*19] the strictly related problem of localization is addressed. They show that by aligning the spectrum of the Hamiltonian on the complete shape with the eigenvalues of the Dirichlet Laplacian on the partial shape, the potential function localizes on the corresponding region. We propose a new pipeline which combines the two approaches obtaining results at the state of the art.

Our reasoning is based on the simple fact that when considering the two approaches in a coupled fashion their weaknesses tend to disappear: namely, a functional map between the two domains needs a well defined region of potential in order to localize the eigenfunctions, while the performance of the localization algorithm heavily depends on the initialization of the potential function, since the spectra alignment technique alone is not good at escaping local minima of the highly nonconvex problem.

Leveraging on the natural relation between the two problems, our algorithm alternates between the optimization for the functional map and the region localization task, converging to accurate results in a fully automatic way. In addition, we noticed that the evolution of the functional map along the optimization problem locally resembles the behavior encountered in the parametric study of the step potential in the previous sections.

8.1. Method

More formally, consider two manifolds $\mathcal{M}$ and $\mathcal{N}$, a functional correspondence $T : \mathcal{L}^2(\mathcal{N}) \to \mathcal{L}^2(\mathcal{M})$, and its matrix representation $\mathbf{C}$ of size $n \times n$, possibly truncated to the first $k \times k$ spectral coefficients. In our approach, $\mathcal{M}$ models the complete shape and $\mathcal{N}$ the partial one, $\mathbf{\Phi}$ is the Hamiltonian basis of $\mathbf{H} = \mathbf{L} + \tau\mathbf{AP}$ on $\mathcal{M}$ and $\mathbf{\Psi}$ is the Dirichlet basis of $\mathbf{L}$ on $\mathcal{N}$.

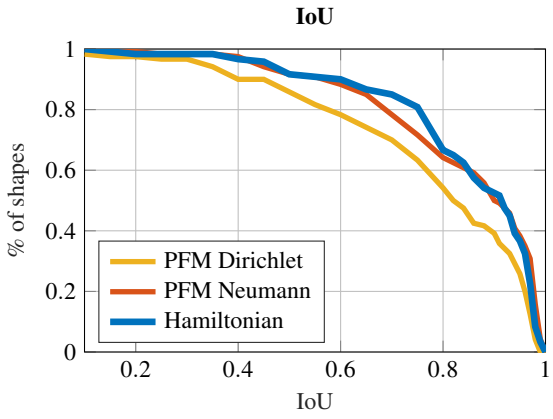

Figure 13: *Comparison of Intersection over Union scores over the region identified by the Hamiltonian functional map framework (in blue) and PFM [RCB*17] with Dirichlet and Neumann boundary conditions (respectively in yellow and red).*

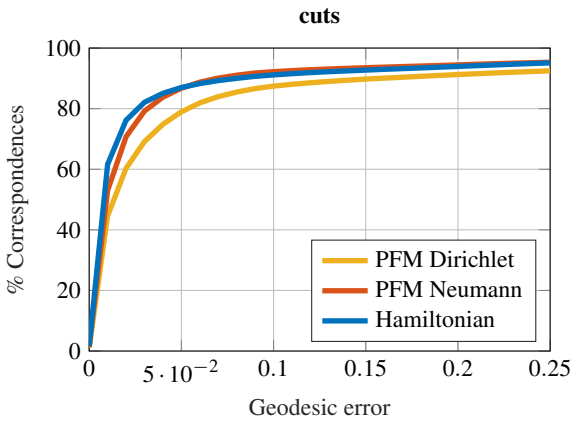

Figure 14: *Correspondence quality comparison with PFM using Dirichlet and Neumann boundary conditions. The error measure is computed according to the Princeton protocol [KLF11].*

Method	mean IOU	median IOU	AUC geod err	AUC IoU
Hamiltonian	**0.837**	**0.914**	**21.959**	**0.74**
PFM Neumann	0.829	0.904	21.910	0.72
PFM Dirichlet	0.761	0.829	20.657	0.66

Table 1: *Performance scores for SHREC 2016: we reach SOTA results (in bold) over mean and median IoU's, and with respect to the area under the geodesic error curves reported in Figure 14.*

In brief, the problem deals with the identification of a region $\mathcal{S} \subset \mathcal{M}$, which corresponds to $\mathcal{N}$. To solve it, we aim at finding the corresponding functional map $\mathbf{C}$ and a potential function $\mathbf{v}$ over $\mathcal{M}$ corresponding to the missing part. Our approach can be summarized in the following four steps, repeated until convergence:

1. Estimate the map $\mathbf{C}$ between $\mathbf{\Psi}$ and $\mathbf{\Phi}$.
2. Initialize the potential function $\mathbf{v}$ by transferring an indicator function $\chi_{\mathcal{N}}$ via $\mathbf{C}$ on $\mathcal{M}$.
3. Optimize $\mathbf{v}$ by aligning the spectra of $\mathbf{H}_{\mathcal{M}}$ and $\mathbf{L}_{\mathcal{N}}$.
4. Recompute $\mathbf{\Phi}$, solving the generalized eigenvalue problem associated with the potential $\mathbf{P} = \mathrm{diag}(\mathbf{v})$.

The first step corresponds to the one proposed in [RCB*17], with the fundamental difference that the map is between the Hamiltonian and the Dirichlet bases, rather than using the Neumann basis. The optimization consists in solving a regularized least squares problem:

$$\arg\min_{\mathbf{C}} ||\mathbf{CA} - \mathbf{B}||_{2,1} + \rho(\mathbf{C}), \tag{34}$$

where $\mathbf{B}$ are the spectral coefficients w.r.t $\mathbf{\Phi}$ of some point descriptors on $\mathcal{M}$, and $\mathbf{CA}$ are the spectral coefficients of the same kind of descriptors on $\mathcal{N}$ transferred to $\mathbf{\Phi}$ via $\mathbf{C}$, while ρ corresponds to regularization terms as defined in [RCB*17]. The third step corresponds to the localization problem in [RTO*19] where we estimate $\mathbf{v}$ by solving

$$\arg\min_{\mathbf{v}} ||\boldsymbol{\lambda}(\mathbf{L}_{\mathcal{M}} + \tau\mathbf{AP}) - \boldsymbol{\mu}(\mathbf{L}_{\mathcal{N}})||_F, \tag{35}$$

where $\boldsymbol{\lambda}$ are the eigenvalues of the Hamiltonian, $\mathbf{H}$ and μ are the eigenvalues of the Laplacian on $\mathcal{N}$ and $||\cdot||_F$ denotes the Frobenius norm. Steps 2 and 4 act as connecting elements between the two minimization problems, with the whole process converging to the alignment of eigenspaces of $\mathbf{H}_{\mathcal{S}}$ and $\mathbf{L}_{\mathcal{N}}$ and the identification of the region itself. Importantly, the map $\mathbf{C}$ will tend to be diagonal and full rank across the iterations, differently from [RCB*17] where the correspondence matrix has a slanted diagonal structure. This follows from Theorem 1. The algorithm is summarized in Appendix B.

8.2. Results

We evaluated our approach on the SHREC 2016 Partiality benchmark [CRB*16] on a set of 120 partial shapes corresponding to nearly-isometric deformations of regions of 8 reference models.

In Figure 14 we plot the Cumulative Match Curve, showing that our method compares favorably with the state of the art [RCB*17], especially in the left part of the curve. This proves that using localized Hamiltonian basis helps in increasing match accuracy and improves the region localization as shown by the higher Intersecion over Union (IoU) curve in Figure 13. In Table 1 we also report comparisons with the method of [RCB*17] in which we just replace Neumann with Dirichlet boundary conditions, showing the benefits of adopting the Hamiltonian basis and simultaneously optimizing the potential and the functional map with the proposed method.

9. Conclusion

In this work we introduced the Hamiltonian functional map formalism and performed a deep theoretical analysis on it to provide a well founded theory to the geometry processing community. Doing so we have emphasized how an attentive theoretical analysis of purely discrete quantities can provide unique insights on the behavior of observed spectral phenomena, which lack a meaningful explanation from the continuous point of view. We have investigated the

possibility of tracking the evolution of eigenfunctions by observing eigenvalue curves (using their veering indices). This allowed us to understand precisely their local geometric transformations (approximated rotations), otherwise difficult to access from the global functional map representation. Paired with the asymptotic behavior, we used these findings to characterize the double diagonal structure of the maps, where each diagonal is related to Hamiltonian eigenfunctions on complementary regions of the mesh that decompose Laplacian eigenfunctions. Additionally, we showed how this formalism is not just limited to the theoretical setting, but it also represents a practical tool, allowing to tackle the partial functional matching problem with a new, unifying approach, which leads to state of the art results on a challenging dataset.

The theoretical contribution opens up new directions in which perturbative methods could be employed in the analysis of geometric optimization algorithms, in settings that could be different from the one approached in this paper. The parametric study, performed here in the case of the step potential, could be taken further, in order to study the behavior of more complex systems such as geometric flows or continuous deformations of manifolds. Finally, the tracking of eigenfunctions along eigenvalue curves using veering indices leaves many possibilities open for exploration.

Acknowledgments

This work was supported by the ERC Starting Grant No. 802554 (SPECGEO) and the MIUR under grant "Dipartimenti di eccellenza 2018-2022" of the Department of Computer Science of Sapienza University. LC was partially supported by the ERC Consolidator Grant No. 724228 (LEMAN).

References

[BAL11] BOIS J. D., ADHIKARI S., LIEVEN N.: On the quantification of eigenvalue curve veering: A veering index. *Journal of Applied Mechanics 78* (07 2011). 2, 6, 7, 8

[BEKB15] BOSCAINI D., EYNARD D., KOUROUNIS D., BRONSTEIN M. M.: Shape-from-operator: Recovering shapes from intrinsic operators. In *Computer Graphics Forum* (2015), vol. 34, Wiley Online Library, pp. 265–274. 2

[CH15] CANZANI Y., HANIN B.: Fixed frequency eigenfunction immersions and supremum norms of random waves. *Electronic Research Announcements 22* (2015), 76. 11

[CPR*19] COSMO L., PANINE M., RAMPINI A., OVSJANIKOV M., BRONSTEIN M. M., RODOLÀ E.: Isospectralization, or how to hear shape, style, and correspondence. In *Proceedings of the IEEE Conference on Computer Vision and Pattern Recognition* (2019), pp. 7529–7538. 2

[CRB*16] COSMO L., RODOLÀ E., BRONSTEIN M. M., TORSELLO A., CREMERS D., SAHILLIOGLU Y.: Shrec'16: Partial matching of deformable shapes. *Proc. 3DOR 2*, 9 (2016), 12. 2, 12

[CRM*16] COSMO L., RODOLÀ E., MASCI J., TORSELLO A., BRONSTEIN M. M.: Matching deformable objects in clutter. In *2016 Fourth International Conference on 3D Vision (3DV)* (2016), IEEE, pp. 1–10. 2

[CSBK18] CHOUKROUN Y., SHTERN A., BRONSTEIN A., KIMMEL R.: Hamiltonian operator for spectral shape analysis. *IEEE Transactions on Visualization and Computer Graphics PP* (08 2018), 1–1. 2

[CT62] CLAASSEN R. W., THORNE C. J.: Vibrations of a rectangular cantilever plate. *Journal of the Aerospace Sciences 29*, 11 (1962), 1300–1305. 2

[DBAL07] DU BOIS J., ADHIKARI S., LIEVEN N.: Experimental and numerical investigation of mode veering in a stressed structure. *Conference Proceedings of the Society for Experimental Mechanics Series* (01 2007). 2

[dBAL09] DU BOIS J. L., ADHIKARI S., LIEVEN N. A. J.: Eigenvalue curve veering in stressed structures: An experimental study. *Journal of Sound and Vibration 322*, 4 (2009), 1117 – 1124. 2

[DPTZ19] DENTON P. B., PARKE S. J., TAO T., ZHANG X.: Eigenvectors from eigenvalues: a survey of a basic identity in linear algebra. arXiv:1908.03795. 5, 14, 15

[FK68] FOX R. L., KAPOOR M. P.: Rates of change of eigenvalues and eigenvectors. *AIAA Journal 6*, 12 (1968), 2426–2429. 5, 14

[GCR*17] GASPARETTO A., COSMO L., RODOLÀ E., BRONSTEIN M., TORSELLO A.: Spatial maps: From low rank spectral to sparse spatial functional representations. In *2017 International Conference on 3D Vision (3DV)* (2017), IEEE, pp. 477–485. 2

[GMT15] GASPARETTO A., MINELLO G., TORSELLO A.: Non-parametric spectral model for shape retrieval. In *2015 International Conference on 3D Vision* (2015), IEEE, pp. 344–352. 2

[Gri94] GRIFFITHS D. J.: *Introduction to Quantum Mechanics*. Prentice Hall, 1994. 4

[GSS99] GUSKOV I., SWELDENS W., SCHRÖDER P.: Multiresolution signal processing for meshes. In *Proceedings of the 26th Annual Conference on Computer Graphics and Interactive Techniques* (USA, 1999), SIGGRAPH '99, ACM Press/Addison-Wesley Publishing Co., p. 325–334. 2

[KBB*13] KOVNATSKY A., BRONSTEIN M. M., BRONSTEIN A. M., GLASHOFF K., KIMMEL R.: Coupled quasi-harmonic bases. *Comput. Graph. Forum 32* (2013), 439–448. 2

[KG01] KARNI Z., GOTSMAN C.: Spectral compression of mesh geometry. *Proceedings of the ACM SIGGRAPH Conference on Computer Graphics 2000* (08 2001). 2

[KGB16] KOVNATSKY A., GLASHOFF K., BRONSTEIN M. M.: Madmm: A generic algorithm for non-smooth optimization on manifolds. In *Computer Vision – ECCV 2016* (Cham, 2016), Leibe B., Matas J., Sebe N., Welling M., (Eds.), Springer International Publishing, pp. 680–696. 2

[KLF11] KIM V., LIPMAN Y., FUNKHOUSER T.: Blended intrinsic maps. *ACM Transactions on Graphics (Proc. SIGGRAPH) 30*, 4 (July 2011). 12

[Lev06] LEVY B.: Laplace-beltrami eigenfunctions towards an algorithm that" understands" geometry. In *IEEE International Conference on Shape Modeling and Applications 2006 (SMI'06)* (2006), IEEE, pp. 13–13. 2

[LJC17] LIU D. H.-T., JACOBSON A., CRANE K.: A dirac operator for extrinsic shape analysis. *Computer Graphics Forum* (2017). 2

[MDSB03] MEYER M., DESBRUN M., SCHRÖDER P., BARR A. H.: Discrete differential-geometry operators for triangulated 2-manifolds. *Visualization and Mathematics III* (2003), 35 – 57. 4

[MRCB17] MELZI S., RODOLÀ E., CASTELLANI U., BRONSTEIN M.: Localized manifold harmonics for spectral shape analysis. *Computer Graphics Forum 37*, 6 (2017), 20–34. 2

[Nel76] NELSON R. B.: Simplified calculation of eigenvector derivatives. *AIAA Journal 14*, 9 (1976), 1201–1205. 5, 8

[NVT*14] NEUMANN T., VARANASI K., THEOBALT C., MAGNOR M., WACKER M.: Compressed Manifold Modes for Mesh Processing. *Computer Graphics Forum* (2014). 2

[OBCS*12] OVSJANIKOV M., BEN-CHEN M., SOLOMON J., BUTSCHER A., GUIBAS L.: Functional maps: A flexible representation of maps between shapes. *ACM Trans. Graph. 31*, 4 (July 2012). 2, 4, 11

[OLCO13] OZOLIŅ V., LAI R., CAFLISCH R. E., OSHER S.: Compressed modes for variational problems in mathematics and physics. *Proceedings of the National Academy of Sciences of the United States of America 110 46* (2013), 18368–73. 2

[PM86] PERKINS N. C., MOTE C. D.: Comments on curve veering in eigenvalue problems. *Journal of Sound and Vibration 106*, 3 (1986), 451 – 463. 2, 5, 6

[RCB*17] RODOLÀ E., COSMO L., BRONSTEIN M., TORSELLO A., CREMERS D.: Partial functional correspondence. *Computer Graphics Forum 36*, 1 (2017), 222–236. 2, 3, 11, 12, 15, 16

[RCL*17] RODOLÀ E., COSMO L., LITANY O., BRONSTEIN M., BRONSTEIN A., AUDEBERT N., HAMZA A. B., BOULCH A., CASTELLANI17 U., DO16 M., ET AL.: Shrec'17: Deformable shape retrieval with missing parts. In *Proceedings of the Eurographics Workshop on 3D Object Retrieval, Lisbon, Portugal* (2017), pp. 23–24. 2

[RLB*19] RODOLÀ E., LÄHNER Z., BRONSTEIN A. M., BRONSTEIN M. M., SOLOMON J.: Functional maps representation on product manifolds. *Computer Graphics Forum 38*, 1 (2019), 678–689. 2

[RTO*19] RAMPINI A., TALLINI I., OVSJANIKOV M., BRONSTEIN A., RODOLÀ E.: Correspondence-free region localization for partial shape similarity via hamiltonian spectrum alignment. In *Proc. 3DV* (2019). 2, 11, 12

[RWP06] REUTER M., WOLTER F.-E., PEINECKE N.: Laplace–beltrami spectra as 'shape-dna' of surfaces and solids. *Computer-Aided Design 38*, 4 (2006), 342 – 366. Symposium on Solid and Physical Modeling 2005. 2

[SS90] STEWART G. W., SUN J.: *Matrix Perturbation Theory*. Computer science and scientific computing. Academic Press, 1990. 14

[Tau95] TAUBIN G.: A signal processing approach to fair surface design. In *Proceedings of the 22Nd Annual Conference on Computer Graphics and Interactive Techniques* (New York, NY, USA, 1995), SIGGRAPH '95, ACM, pp. 351–358. 2

[ZTZ13] ZIENKIEWICZ O., TAYLOR R., ZHU J.: *The Finite Element Method: Its Basis and Fundamentals*. The Finite Element Method. Elsevier Science, 2013. 2

A. Theorem proofs

Lemma 1 (Weyl's inequality [SS90]) Let $\mathbf{X}$ and $\mathbf{Y}$ be two real symmetric matrices with eigenvalues $\xi_1 \leq \ldots \leq \xi_n$ and $\upsilon_1 \leq \ldots \leq \upsilon_n$, respectively. Let $\mathbf{Z} = \mathbf{X} + \mathbf{Y}$ with eigenvalues $\zeta_1 \leq \ldots \leq \zeta_n$. Then, for each i:

$$\xi_i + \upsilon_1 \leq \zeta_i \leq \xi_i + \upsilon_n \,. \tag{36}$$

Theorem 2 Following [FK68], the derivatives of the eigenvalues λ_i and of the eigenvectors ψ_i in a generalized symmetric eigensystem, with mass matrix $\mathbf{A}$ and stiffness matrix $\mathbf{K}$ (dependent on a parameter τ) are given by:

$$\frac{d}{d\tau}\lambda_i = \psi_i^T \left(\frac{d}{d\tau}\mathbf{K} - \lambda_i \frac{d}{d\tau}\mathbf{A} \right) \psi_i \tag{37}$$

$$\frac{d}{d\tau}\psi_i = -\frac{\psi_i^T \left(\frac{d}{d\tau}\mathbf{A}\right)\psi_i}{2} + \sum_{j \neq i} \frac{\psi_j^T \left(\frac{d}{d\tau}\mathbf{K} - \lambda_i \frac{d}{d\tau}\mathbf{A}\right)\psi_i}{\lambda_i - \lambda_j} \psi_j \,. \tag{38}$$

In our setting $\mathbf{K} = \mathbf{W} + \tau\mathbf{AP}$ (reference Eq. (9)). Differentiating the two matrices we obtain:

$$\frac{d}{d\tau}\mathbf{K} = \mathbf{AP} \tag{39}$$

$$\frac{d}{d\tau}\mathbf{A} = \mathbf{0} \,. \tag{40}$$

Substituting Eqs. (39) and (40) in Eq. (37) we obtain the eigenvalue derivative:

$$\frac{d}{d\tau}\lambda_i = \psi_i^T \mathbf{AP} \psi_i \,. \tag{41}$$

Substituting Eqs. (39) and (40) in Eq. (38) we obtain the eigenvector derivative:

$$\frac{d}{d\tau}\psi_i = \sum_{j \neq i} \frac{\psi_j^T \mathbf{AP} \psi_i}{\lambda_i - \lambda_j} \psi_j \,. \tag{42}$$

Now we can compute the second eigenvalue derivative by differentiating Eq. (41) and using Eq. (42):

$$\frac{d^2}{d\tau^2}\lambda_i = 2 \sum_j a_{ii} p_{ii} \psi_{ij} \frac{d}{d\tau}\psi_{ij} \tag{43}$$

$$= 2 \left(\frac{d}{d\tau}\psi_i \right)^T \mathbf{AP} \psi_i \tag{44}$$

$$= 2 \left(\sum_{j \neq i} \psi_j^T \frac{\psi_j^T \mathbf{AP} \psi_i}{\lambda_i - \lambda_j} \right) \mathbf{AP} \psi_i \tag{45}$$

$$= 2 \sum_{j \neq i} \frac{(\psi_j^T \mathbf{AP} \psi_i)^2}{\lambda_i - \lambda_j} \,. \tag{46}$$

Proposition 1 Let $\delta\tau = \tau_2 - \tau_1$. We can write $\mathbf{H}_2 = \mathbf{H}_1 + \delta\tau\mathbf{P}$. Let us apply Lemma 1, setting $\mathbf{X} = \mathbf{H}_1$ and $\mathbf{Y} = \delta\tau\mathbf{P}$. We get:

$$\lambda_{i1} \leq \lambda_{i2} \leq \lambda_{i1} + \delta\tau \,. \tag{47}$$

Theorem 3 The first task is to bound asymptotically the eigenvalues of the Hamiltonian matrix using Lemma 1. We set $\mathbf{Y} = \mathbf{A}^{-1}\mathbf{W}$ and $\mathbf{X} = \tau \mathrm{diag}(\mathbf{v}) = \tau\mathbf{P}$. Since $\mathbf{X}$ has the first r eigenvalues equal to 0 and the subsequent ones equal to τ, we get:

$$\mu_1 \leq \lambda_i \leq \mu_n \tag{48}$$

$$\tau + \mu_1 \leq \lambda_j \leq \tau + \mu_n \,. \tag{49}$$

Equation (48) tells us that the eigenvalues λ_i are bounded from above. Since all eigenvalue curves are increasing (Proposition 1), λ_i converges. From Eq. (49) instead we note that λ_j diverges. Similar inequalities hold for the eigenvalues of the principal minors, with the only difference being the size of the bound given by the minimum and maximum eigenvalue of the Laplacian minor. Therefore, the first $r-1$ (if $p_{ii} = 0$) or r (if $p_{ii} = 1$) eigenvalues of the minors converge while the others diverge. In order to compute $\lim_{\tau \to +\infty} \frac{d}{d\tau}\lambda_i$ and $\lim_{\tau \to +\infty} \frac{d}{d\tau}\lambda_j$ we use Eq. (41), with $\mathbf{A} = \mathbf{I}$ (we are requiring this form since we need unit eigenvectors with respect to the canonical norm):

$$\frac{d}{d\tau}\lambda_h = \psi_h^T \mathbf{P} \psi_h \,. \tag{50}$$

In order to perform the limit on Eq. (50) we should know the asymptotic behaviour of the eigenvectors. We can use the recently celebrated result in [DPTZ19] to write the square of the eigenvector coefficients as a function of the eigenvalues

$$\psi_{hk}^2 = \frac{\prod_{l=1}^{n-1} \lambda_h - \lambda_l^k}{\prod_{l \neq h}^{n} \lambda_h - \lambda_l} \,, \tag{51}$$

where λ_l^k is the l-th eigenvalue of $\mathbf{H}_k$, the k-th principal minor of $\mathbf{H}$. First we concentrate on the terms ψ_{ik} such that $\mathbf{P}_{kk} = 1$:

$$\psi_{ik}^2 = \frac{\prod_{l=1}^{n-1} \lambda_i - \lambda_l^k}{\prod_{l=1, l\neq i}^{n} \lambda_i - \lambda_l} \tag{52}$$

$$= \frac{\prod_{l=1}^{n-1} \lambda_i - \lambda_l^k}{\prod_{l=1, l\neq i}^{r} \lambda_i - \lambda_l \prod_{l=r+1}^{n} \lambda_i - \lambda_l} \tag{53}$$

$$= \frac{\prod_{l=1}^{r} \lambda_i - \lambda_l^k}{\prod_{l=1, l\neq i}^{r} \lambda_i - \lambda_l} \frac{\prod_{l=r+1}^{n-1} \lambda_i - \lambda_l^k}{\prod_{l=r+1}^{n} \lambda_i - \lambda_l} \tag{54}$$

$$= \frac{\prod_{l=1}^{r-1} \lambda_i - \lambda_l^k}{\prod_{l=1, l\neq i}^{r} \lambda_i - \lambda_l} (\lambda_i - \lambda_r^k) \frac{\prod_{l=r+1}^{n-1} \lambda_i - \lambda_l^k}{\prod_{l=r+1}^{n-1} \lambda_i - \lambda_l} \frac{1}{\lambda_i - \lambda_n} . \tag{55}$$

In each sum we recognize four terms and λ_i is present in each of them. For $\tau \to +\infty$, λ_i tends to a finite value l_i. Let us take the limit on each term. The first term is a fraction containing the same number of factors on the numerator and on the denominator. Both λ_l^k and λ_l tend to finite values l_l and l_l^k. The only problem can arise if $l_i = l_l$, when $\lambda_i - \lambda_l \to 0$. To this end, we make use of Cauchy's interlacing inequalities [DPTZ19]:

$$\lambda_i \leq \lambda_i^k \leq \lambda_{i+1} . \tag{56}$$

Using this result we have that $\lambda_i \leq \lambda_l^k \leq \lambda_l$ or $\lambda_l \leq \lambda_l^k \leq \lambda_i$. In both cases it holds:

$$|\lambda_i - \lambda_l^k| \leq |\lambda_i - \lambda_l| , \tag{57}$$

so

$$\frac{\lambda_i - \lambda_l^k}{\lambda_i - \lambda_l} \in [-1, 1] . \tag{58}$$

With this, we establish that the first term is bounded. The second term is bounded as well. The third term has a structure reminiscent of the first term but now λ_l and λ_l^k tend to $+\infty$. Using Eq. (49) we can write each fraction as:

$$\frac{\lambda_i - \lambda_l^k}{\lambda_i - \lambda_l} = \frac{\lambda_i - (\tau + \alpha_1)}{\lambda_i - (\tau + \alpha_2)} \tag{59}$$

for $\alpha_1, \alpha_2 \in [\mu_1, \mu_n]$ It is clear that each one of these terms converges to 1. Finally, the last term tends to 0. Wrapping it up, the last zero limit dominates the product so we obtain:

$$\lim_{\tau \to +\infty} \psi_{ik}^2 = 0 . \tag{60}$$

Now we limit the coefficients ψ_{jk} with $\mathbf{P}_{kk} = 0$. Proceeding as in Eqs. (52)-(54), we obtain:

$$\psi_{jk}^2 = \frac{\prod_{l=1}^{r-1} \lambda_j - \lambda_l^k}{\prod_{l=1}^{r-1} \lambda_j - \lambda_l} \frac{1}{\lambda_j - \lambda_r} \frac{\prod_{l=r}^{n-2} \lambda_j - \lambda_l^k}{\prod_{l=r+1, l\neq j}^{n} \lambda_j - \lambda_l} (\lambda_j - \lambda_n^k) . \tag{61}$$

By Eq. (49) we write $\lambda_j = \tau + \alpha_j$, $\lambda_l = \tau + \alpha_l$ for $l \geq r+1$ and $\lambda_l^k = \tau + \alpha_l^k$ for $l \geq r$, with $\alpha_j, \alpha_l, \alpha_l^k \in [\mu_1, \mu_n]$. Rewriting Eq. (61)

$$\psi_{jk}^2 = \frac{\prod_{l=1}^{r-1} \tau + \alpha_j - \lambda_l^k}{\prod_{l=1}^{r-1} \tau + \alpha_j - \lambda_l} \frac{1}{\tau + \alpha_j - \lambda_r} \frac{\prod_{l=r}^{n-2} \alpha_j - \alpha_l^k}{\prod_{l=r+1, l\neq j}^{n} \alpha_j - \alpha_j} (\alpha_j - \alpha_n^k) . \tag{62}$$

The first term tends to 1, the second term tends to 0, the third term

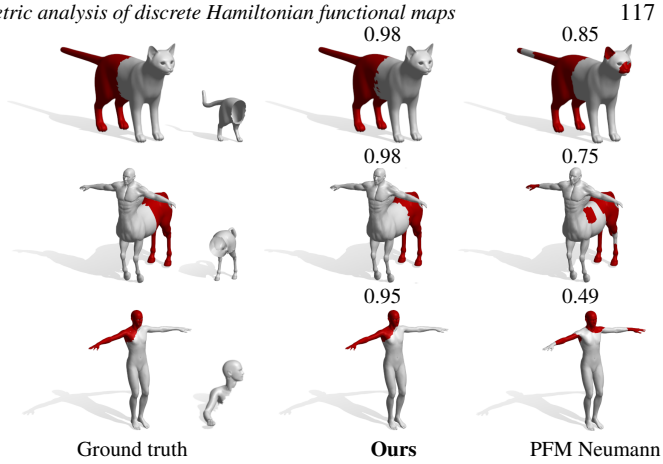

Figure 15: *Qualitative comparison of the localized region (in red) on the full shape corresponding to an near-isometric deformation of the queried partial shape. Left: Ground truth regions and corresponding partial shapes. Center: our result computed with algorithm 1. Right: Results of [RCB*17] with Neumann b.c.. On the top of each results are reported the IOU scores w.r.t. the ground truth regions.*

can be bounded following Eqs. (56)-(58) (since $\alpha_j, \alpha_l, \alpha_l^k$ converge in $[\mu_1, \mu_n]$) while the last term tends to a finite value. We have:

$$\lim_{\tau \to +\infty} \psi_{jk}^2 = 0 . \tag{63}$$

Combining Eqs. (50) and (60),

$$\lim_{\tau \to +\infty} \frac{d}{d\tau} \lambda_i = \lim_{\tau \to +\infty} \psi_i^T \mathbf{P} \psi_i = \lim_{\tau \to +\infty} \sum_k \psi_{ik}^2 = 0 . \tag{64}$$

At the same time, since ψ_j is an unit eigenvector,

$$\sum_{k=1}^{n} \psi_{jk}^2 = 1 . \tag{65}$$

Using Eq. (63),

$$\lim_{\tau \to +\infty} \sum_{k:\mathbf{P}_{kk}=1} \psi_{jk}^2 = 1 . \tag{66}$$

We conclude that:

$$\lim_{\tau \to +\infty} \frac{d}{d\tau} \lambda_j = \lim_{\tau \to +\infty} \psi_j^T \mathbf{P} \psi_j = \lim_{\tau \to +\infty} \sum_{k:\mathbf{P}_{kk}=1} \psi_{jk}^2 = 1 . \tag{67}$$

Proposition 2 First we need to prove that $\leq$ is a preorder relation on $\mathcal{C}$. Thus, the reflexive and transitive properties must hold.

- Reflexivity: $\gamma_1 \leq \gamma_1 \iff |i_{11} - i_{12}| \leq |i_{11} - i_{12}| \iff 0 \leq 0$.
- Transitivity: if $\gamma_1 \leq \gamma_2$ and $\gamma_2 \leq \gamma_3$ then $|i_{11} - i_{12}| \leq |i_{21} - i_{22}|$ and $|i_{21} - i_{22}| \leq |i_{31} - i_{32}|$. Combining the two equations we get $\gamma_1 \leq \gamma_3$.

Now we show that a maximum exists. Suppose a maximum does not exist. There must exist two distinct upper bounds γ_1 and γ_2 such that γ_1 is the intersection between σ_{11} and σ_{12} and γ_2 is the intersection between σ_{21} and σ_{22}. Since the bounds are distinct it must be that $\sigma_{11} \neq \sigma_{12} \neq \sigma_{21} \neq \sigma_{22}$. Let $i_{31} = \min\{i_{11}, i_{12}, i_{21}, i_{22}\}$,

Algorithm 1 Partial Hamiltonian functional map

Require:

- A complete shape $\mathcal{M}$
- A partial shape $\mathcal{N}$, s.t. $\mathcal{N}$ is an isometric deformation of some $\mathcal{S} \subset \mathcal{M}$
- $\mathbf{A}$: a set of point descriptors on $\mathcal{N}$
- $\mathbf{B}$: a set of point descriptors on $\mathcal{M}$

1: **for** $k = 1 \dots end$ **do**
2: $\quad \mathbf{C}_k \leftarrow \arg\min_{\mathbf{C}} ||\mathbf{CA} - \mathbf{B}||_F + \rho(\mathbf{C})$
3: $\quad \mathbf{v}_{init} \leftarrow \mathbf{\Phi}_k \mathbf{C}_k \mathbf{\Psi}^T \mathbf{A}_{\mathcal{N}} \boldsymbol{\chi}_{\mathcal{N}}$
4: $\quad \mathbf{v}_k \leftarrow \arg\min_{\mathbf{v}} ||\boldsymbol{\lambda}(\mathbf{L}_{\mathcal{M}} + \tau\mathbf{AP}(\mathbf{v})) - \boldsymbol{\mu}(\mathbf{L}_{\mathcal{N}})||_F$
5: $\quad \mathbf{\Phi}_k \leftarrow (\mathbf{L}_{\mathcal{M}} + \tau\mathbf{AP})\mathbf{\Phi} = \mathbf{\Lambda}\mathbf{\Phi}$
6: **end for**
7: **return** $\mathbf{C}_{end}, \mathbf{v}_{end}$

$i_{32} = \max\{i_{11}, i_{12}, i_{21}, i_{22}\}$ and set γ_3 as the intersection between σ_{31} and σ_{32}. Now, by construction it holds $|i_{11} - i_{12}| \leq |i_{31} - i_{32}|$ and $|i_{21} - i_{22}| \leq |i_{31} - i_{32}|$, meaning that $\gamma_1 \leq \gamma_3$ and that $\gamma_2 \leq \gamma_3$, proving the thesis by contradiction.

B. Algorithmics

In Algorithm 1 we report our pipeline to tackle partial functional mapping exploiting the Hamiltonian functional map formalism. Lines 2 and 4 of the algorithm are computed using standard conjugate gradient methods (projected onto the space of positive functions for the latter). Line 3 of the algorithm serves as an initialization of the non-convex problem on the following line. Termination criteria are set according to the geodesic error of the current estimate of the map $\mathbf{C}_k$.

In Figure 15 we show a qualitative comparison for the region localized with Algorithm 1 (the complementary region of the potential function v): comparing with [RCB*17] our approach seems to promote more contiguous regions, obtaining better results in cases with symmetric sub-matches (e.g. the arms and hands of the human model in the last row).